

# Progress report of the AEGIS experiment (2021)

## The AEGIS/AD-6 collaboration

The AEGIS experiment [1] is designed around the goal of measuring the behaviour of antimatter in the Earth's gravitational field. The experimental protocol is based on the pulsed production of a beam of antimatter atoms, launched horizontally, and measuring the gravity-induced vertical displacement of these antimatter atoms by means of a position-sensitive detection device based on gratings and a high-spatial resolution detector. Pulsed formation of antihydrogen is based on the charge exchange process:



A crucial figure of merit for the measurement is  $N_{det}$ , the number of atoms reaching the detector; the divergence of the formed beam is determined by the temperature (and space charge) of the antiprotons, and the efficiency of the beam formation mechanism. Furthermore, for identical divergence, reaching higher sensitivity greatly benefits from lower velocities.

In the years leading up to LS2, AEGIS had worked towards validating the steps required for the pulsed formation of Rydberg antihydrogen atoms, and had achieved this goal at the end of 2018 [2]. In 2019, in the absence of antiprotons, we had focused on working with positrons and positronium, relying on one hand on measurements carried out in 2018 within the 1T cryostat, and on the other hand on the dedicated external positronium test setup, while at the same time launching an in-depth review of the physics program and technology changes required to achieve the significant advances that are outlined in the report [3] submitted to the SPSC in Nov. 2019 that details the long term physics goals and related work for AEGIS.

After having focused during that part of 2020 that was possible given the Covid-19 situation in that year on pursuing the developmental work with positronium and preparing and implementing the necessary modifications to the apparatus and the experimental area to work towards our long-term physics goals, the the objective for 2021 was then to complete these modifications and the experimental area. The overall boundary conditions however, while better than 2020, continued to be strongly defined by the ongoing Covid-19 situation, with very strong competition for access to CERN's technical facilities and the difficulty for external participants to be actively involved during large stretches of 2021. In spite of a resulting delay (which lies between 3 and 6 months, depending on the specific area) with respect to our initial planning for LS2, thanks to subsequent re-prioritization of several activities (detailed below), we were in a position to test the majority of our new key technologies with antiprotons from ELENA in November 2021. This report will focus on those advances that could be achieved as well as the ongoing modifications to the experimental zone and the apparatus.



## Modifications to the experimental zone in 2021

Several major modifications to the experimental environment in which the experiment is sited, and that were re-prioritized to the beginning of 2021, have been completed. Among these, the most important is the connection to ELENA; in 2019, the installation of the part outside of the AEGIS experimental zone was completed; installation of the final part of the LNE-01 transfer line (inside the AEGIS experimental area) was contingent on removal of the full positron apparatus and a downstream shift of the existing laser hut by 40 cm. Given the active physics program with positronium in 2020, this dismantling and re-assembly that was initially foreseen for summer 2020, after the positron physics run's scheduled completion, started in October 2020 due to the interruption of the positronium physics program by the Covid-19 situation in the first half of the year. In November and early December of 2020, almost all of the remainder of the LNE-01 transfer line was installed (with the exception of a gate valve); reinstallation of the accumulator system above the new transfer line (Fig. 1) began in January of 2021 and was completed in late spring. In the course of this intervention, servicing, refurbishment or replacement of a number of sub-elements was carried out, and an additional safety exit was integrated into the experimental area, which is expected to lead to a safer working environment and better maintainable operation of the positron part of the experiment.

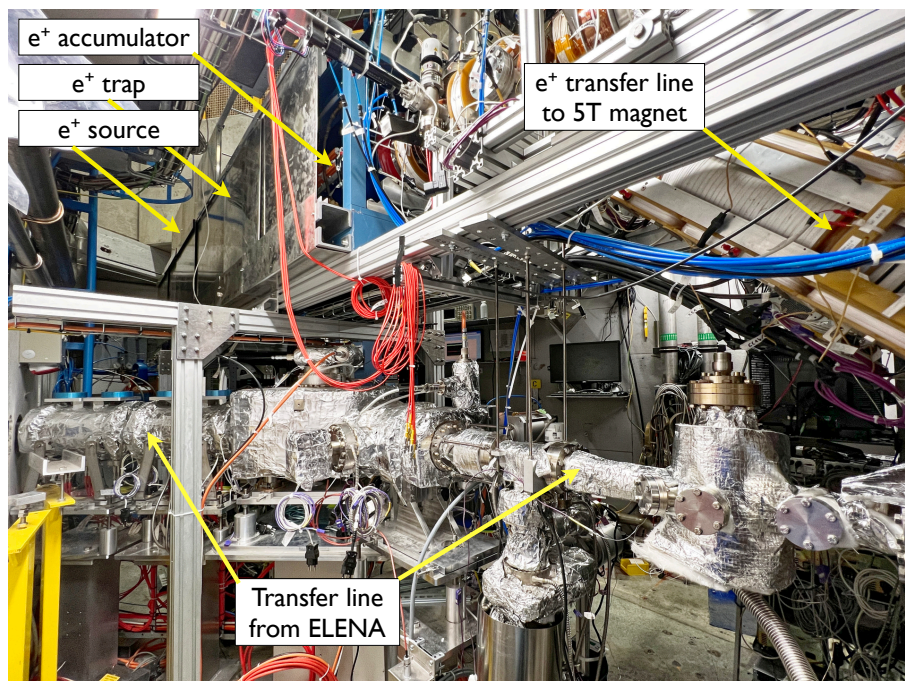


**Figure 1.** Photo of the reassembled and improved positronium set-up above the LNE antiproton transfer line. View from the source towards the 5T magnet.

As detailed in the expanded physics program [3] of AEGIS, laser manipulations play an increasingly important role in the different sub-activities, leading to the need for additional space for the corresponding laser systems. Given the spatial constraints of the AEGIS experimental area, and the withdrawal of the ATRAP experiment, we had asked for and obtained the area formerly used by ATRAP for their positron system, with the intention to install there a large laser hut to house the AEGIS laser systems. However, due to the Covid-19 situation, and the delayed refurbishment activities of the AD magnets below this zone, installation of the laser hut

had to be delayed to spring 2021; in order avoid any risks to the physics program, we have thus decided to re-prioritize the work on the existing laser systems, leaving the current laser systems in their existing position for 2022 (at least), and instead commenced by installing only new laser systems (details are given in a dedicated section below) in the new laser hut (Fig. 2).



**Figure 2.** Left: photo of the new laser hut above the AEgIS experimental area and of the UV transfer line into the experiment; Right: photo of the interior of the laser hut and of the new Alexandrite laser system.

### Modifications to the apparatus in 2021

While a number of design developments could take place in 2020, the need to benefit maximally from whatever time windows became available for essential interventions in the experimental zone and the very reduced availability of manpower overall resulted in less rapid progress than initially foreseen. In particular, convergence of designs and drafting of resulting changes was very negatively affected by the difficulty of carrying out face-to-face discussions and of having rapid turn-around. Six main areas of modifications have nonetheless converged and production of the corresponding items has been completed or is close to completion. These concern a re-design of the antihydrogen production region to reflect the need for higher antihydrogen production rates; a greatly improved Ps laser excitation diagnostic scheme; a novel very low energy antiproton degrading and beam position monitoring device; a redesigned entrance region into the 5T trapping magnet; improvements to electric shielding in the antihydrogen formation region to achieve significantly lower antihydrogen temperatures; and a redesign of the central scintillating fiber tracker's (FACT) anticryostat, to allow a much larger sensitive area for a grating / upgraded position sensitive device.

Given the continued Covid-19 related difficulties, we have chosen to focus in 2021 on the fabrication and testing of those elements that were critical to the tests that the short antiproton beam time allowed (entrance region, degrader, FACT anticryostat, electric shielding) and to complete and install the re-designed antihydrogen production region before the 2022 antiproton beam time. Nevertheless, also here, prototyping of several critical elements, among them the

fiber bundle for monitoring of the IR and UV Ps excitation laser pulses and the miniaturized Ps production target needed to be carried out in 2021, and are reported on below.

### *Redesigned entrance region*

The construction of the entrance region was completely redesigned and rebuilt to allow greater reliability of operation, reduced heat flow and adaptation of the beam position monitor (final degrader) to the much lower  $\bar{p}$  energies of ELENA while meeting the boundary condition of very limited space in the 5T magnet entrance region. Figure 3 shows a sketch of the main elements of the inner structure that provides (via two gear systems) access to the beam position monitor (that is moved laterally when injecting positrons or, in the future, ions) and the imaging MCP (that is flipped horizontally when not in use). A mirror (for camera imaging of the MCP) is coupled to the same gear mechanism as the MCP such that they move in and out of the beam axis simultaneously. Improved thermal shields and bellows reduce the heat flow to the liquid He and liquid nitrogen baths. A variable thickness degrader, placed on an actuator slightly upstream of this assembly, allows tuning the antiproton range curve in 100 nm (Parylene N) steps.

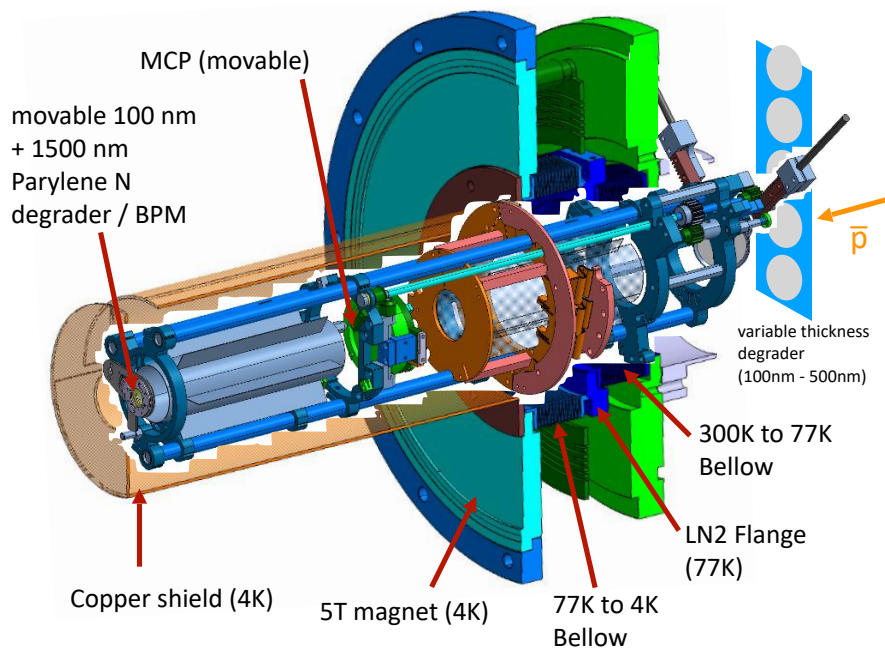


**Figure 3.** Sketch of entrance region apparatus

Positrons are injected onto the apparatus axis slightly upstream of the variable thickness degrader; work is ongoing to modify the beam pipe connecting AEGIS to ELENA. This modified beam pipe, which is foreseen to be installed in spring, will allow injecting ions (specifically, anions) into AEGIS.

### *Beam monitor / degrader for 100 keV antiprotons*

To be able to degrade the antiprotons delivered by ELENA at 100 keV to an energy that allows them to be trapped by the AEGIS apparatus ( $< 10$  keV), thin foils of various materials were investigated via a Geant4 simulation. Given the importance of being able to tune the overall degrader thickness over a rather large range (due to uncertainties inherent in the Geant4 simulation), we chose to focus on the investigation of Parylene N, which, in addition to having low  $Z$  and density (the chemical composition of Parylene is  $C_8H_8$ , and its density is  $1.1$  g/cm<sup>3</sup>) can be fabricated in thin foils with a minimal thickness of 100 nm, and can furthermore be thinly coated (10 nm Al layer thickness) via metal evaporation.

While antiprotons delivered by the AD have sufficient energy to permit using a thin ( $50$   $\mu$ m) silicon pixel detector as beam position monitor (in addition to a total degrader thickness of  $\sim 160$   $\mu$ m Aluminum), this is no longer possible with the 100 keV antiprotons delivered by ELENA. To nonetheless obtain a shot-by-shot monitor of the antiproton beam position and intensity, the final degrader (in total, 1600 nm Parylene N foil) was divided into two, independently metalized foils: a first thicker (1500 nm) foil coated with a four-fold segmented 10 nm Aluminum layer (Fig. 4); and a second, 100 nm foil that is fully coated with 10 nm of Aluminum. The segments are separated by a 1mm gap, forming an uncoated central cross through which the antiprotons nominally pass; any deviation of the beam from its nominal position will cause (part of) it to pass through a metalized sector, thus providing a (rough) positional signal. The second (thin) foil provides a position-independent intensity signal that allows monitoring the passage of the antiprotons independent of the exact beam alignment and that furthermore functions as a Faraday cup for charged particles trapped in the 5T magnet's Penning trap. Both unamplified and amplified (cryogenic amplifiers placed on a PCB in the immediate vicinity of the foils) are transferred via a 1m coaxial cable to vacuum feedthroughs, where the signal is then digitized.

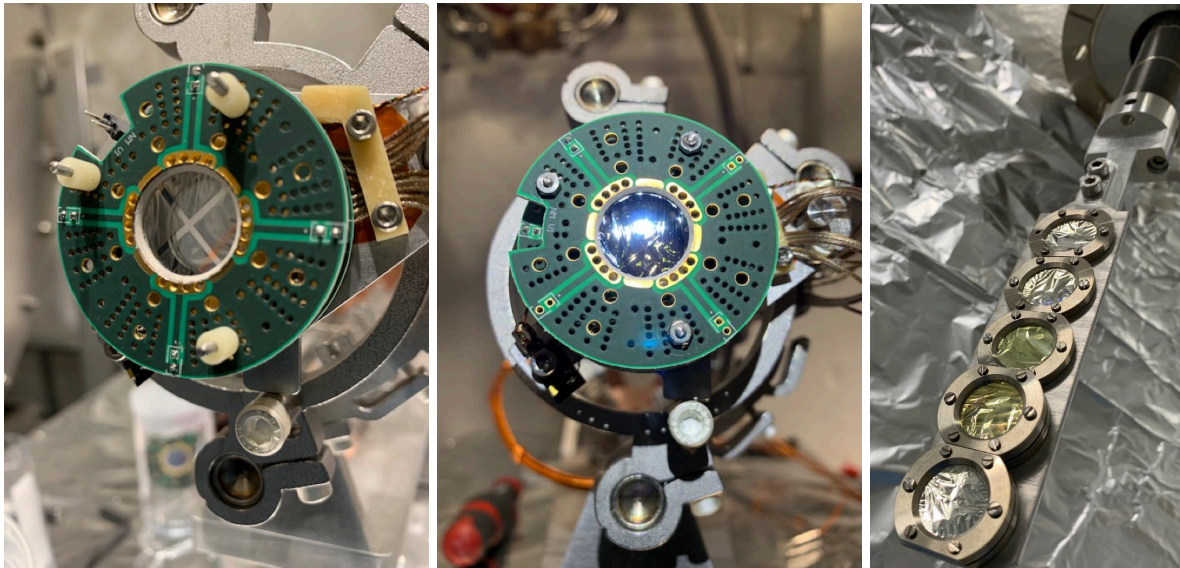


**Figure 4.** Left and center: Photo of the segmented Parylene N degrader foil / PCB assembly (left: 1500 nm segmented foil; center: 100 nm foil); Right: ladder for the 100 nm  $\sim$  500 nm Parylene N foil  $\bar{p}$  range curve fine tuning.

This design was tested in 2021 in two independent beam tests: in a first test at CERN's IRRAD facility consisting of a long sequence of 400 ms spills, each containing  $6 \times 10^{11}$  protons, all four sectors of the four-fold segmented detector were read out; Fig. 5 (top) shows the measured current as a function of time, both for one of the sectors of the segmented foil detector, as well

as for a test beam telescope detector. In a second test, signals from the segmented degrader foil were exposed to the antiproton pulses extracted from ELENA (bottom figure in Fig. 5); the base-line shift at  $-11 \mu\text{s}$  is in temporal coincidence with the  $\sim 150 \text{ ns}$  long pulse of  $\sim 10^7$  antiprotons passing through the corresponding sector.

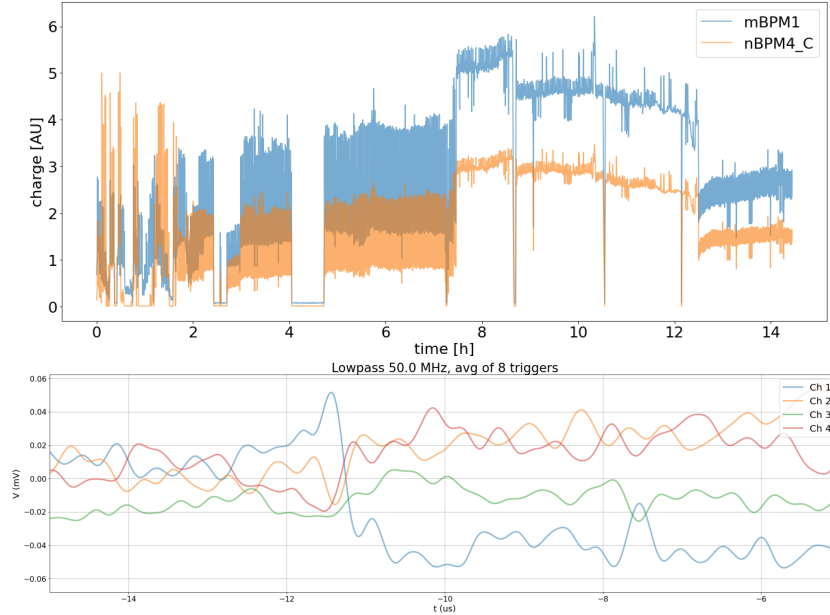


**Figure 5.** Top: signal (nBPM4C, one segment) from an irradiation test of a segmented 1500 nm thick Parylene N (10 nm Al) foil with protons ( $6 \times 10^{11}$  p/spill, 400 ms) at the CERN IRRAD facility (orange line). The blue line corresponds to the current in one of the beam telescope detectors; Right: digital scope signal of all four sectors from an identical foil exposed to 100 keV  $\bar{p}$ 's passing through one of the four sectors (the blue sector).

### *Prototyping of the miniaturized Ps target / fabrication of the fiber bundle*

The major change of the AEGIS experimental apparatus follows a large number of improvements that are being implemented in order to significantly increase the production rate of antihydrogen by charge exchange. This requires both reducing the velocity of formed positronium as well as increasing the principal quantum number of Rydberg positronium able to interact with nearby antiprotons. While the former would not require major changes in geometry, the later does: in order to increase the principal quantum number at which positronium field-ionizes as it traverses the axial magnetic field, the positronium formation target needed to be placed on axis, a choice that affords further advantages (larger electrode radii and possibly closer proximity of antiprotons to the positronium formation target) but also implies the loss of a small solid angle in the downstream direction into which a beam of antihydrogen will need to travel. This loss is minimized by reducing the diameter of the target to a few mm. Diagnostic requirements also mean that the target (purple structure in Fig. 6), as well as a downstream field-ionizing mesh to characterize the formed antihydrogen atoms (pink mesh immediately downstream of the target) need to be movable under operating conditions (cryogenic temperatures, UHV, B-field). Furthermore, while increasing the radial dimensions of the electrodes in the 1T region and removing the anisotropy stemming from radial injection of

Rydberg positronium both are beneficial in reducing heating of trapped antiprotons, imperfect alignment between the magnet's axis and the electrodes' axis mean that electric and magnetic field in the antiproton Penning trap used for the first pulsed formation of antihydrogen [2] may not have been perfectly aligned, which may have led to an additional heating of the antiprotons due to faster expansion of the plasma. This is the rationale for incorporating two cryogenic actuators (two knobs positioned at  $210^\circ$  and  $330^\circ$  in Fig. 6) with which much more accurate alignment at cryogenic temperatures between those two fields in the current design can be achieved. All cryogenic actuators were procured in 2021.

In 2021, a new on-axis Ps production target (see Fig. 7) was prototyped; it consists of a 3D printed titanium support structure/holder which incorporates a heater, a thermal sensor and the 1mm thick,  $5\times 5$  mm square nanostructured Si target itself; this will be incorporated in the new assembly for the 2022 antiproton beam time. The full assembly itself is mounted within the rotatable purple target holder ring structure in Fig. 6.

In order to monitor the position and overlap of the two positronium excitation lasers, we had previously relied on photoconverted light produced by the lasers in a MACOR(TM) screen positioned close to the positronium production target and that could be imaged along the path of the lasers. To improve the diagnostics and avoid the possibility of laser-desorbing any atoms or molecules potentially adsorbed on such a screen, we have redesigned the laser diagnostic system by installing an almost completely reflecting prism assembly (blue structures along the red laser path in Fig. 6), which has the additional benefit of doubling the laser intensity seen by the positronium atoms produced in the target. The small fraction of light that is not retro-reflected reaches a matrix of 800 optical fibers (the black square in Fig. 6 corresponding to the end plane of the fiber array) which carry the residual laser light towards two dedicated imaging cameras (UV and IR) sited outside of the apparatus. Fig. 7 shows the bundle of 800 fibers that will be incorporated in the new assembly for the 2022 antiproton beam time, as well as an image obtained by shining a laser light onto the polished end of the array.

The design illustrated in Fig. 6 incorporates all of the changes indicated above and satisfies all requirements for the upcoming physics program.

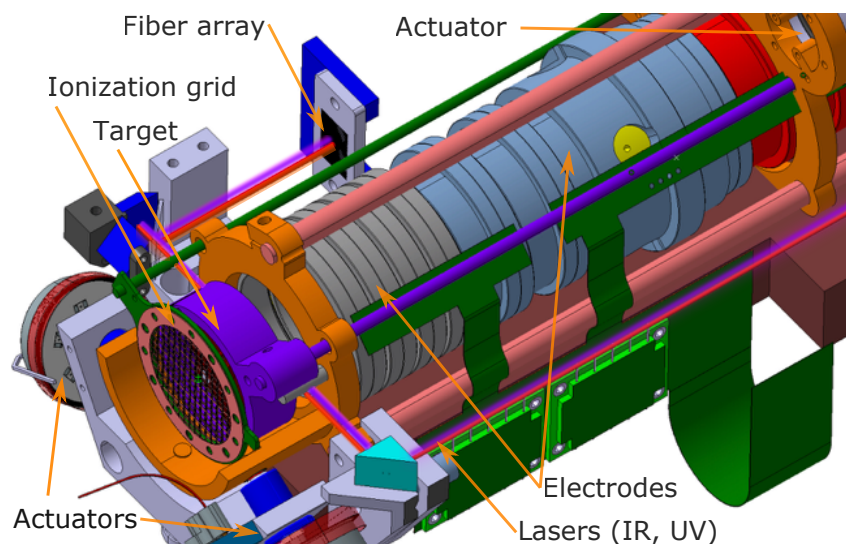


**Figure 6.** New design of the AEGIS antihydrogen production region (the miniature Ps target is sited within the 30 mm diameter ring structure labeled "target"). Images of several of the elements of the new design are shown in Figure 7.

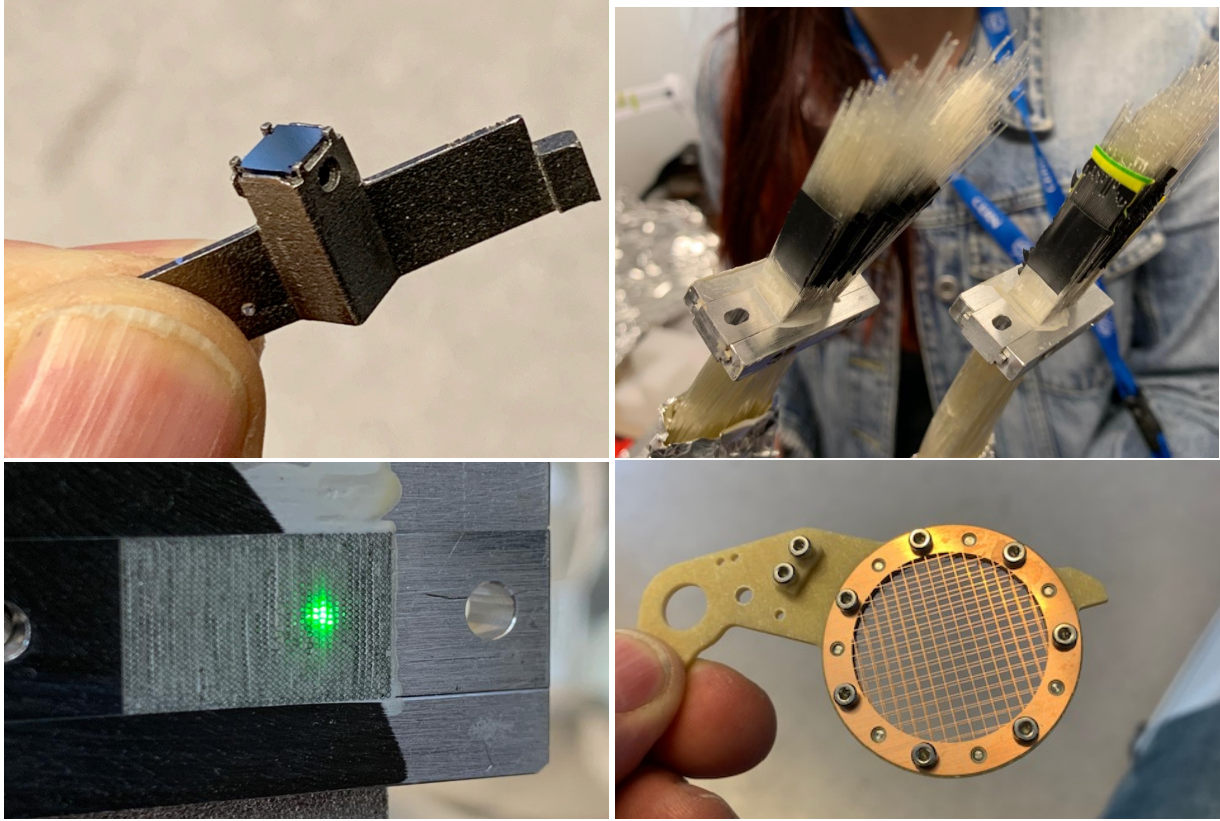


**Figure 7.** Picture of the new on-axis Ps target and holder; picture of UV & IR imaging fiber bundle (during construction), image of a laser pointer on end face of cut/polished fiber bundle (fiber separation = 0.32 mm); picture of the (movable) Rydberg-atom ionization grid (Cu-Be etching technique).

#### *FACT anticryostat and downstream detection*

Several modifications to this region have been completed or are close to completion. In addition to the modifications related to the electrodes in the antihydrogen production region, also the downstream MCP-based imaging detector was completely rebuilt, now allowing a full view of the inside region of the electrodes (whose diameter is now constant across the full apparatus). This detector has been crucial in imaging the antiproton beam (and thus in steering) in 2021. In order for this detector to be accordingly adapted, a constriction in the anticryostat housing the FACT scintillating fiber tracker needed to be removed, requiring a redesign of this anticryostat as well as electron beam welding of the stainless steel enclosure with the fiber detector in place.

#### *Modifications to the laser system (new laser, UV laser transport line)*

In 2021, we developed and implemented a single pulse use modality for all laser systems. This allows extending the lifetime of all optical components thus reducing the maintenance costs and efforts. Work towards higher energy in the UV has been carried out as well as implementing diagnostics for the spectral properties of the lasers with higher resolution.

A new laser system composed of two independent oscillators emitting between 729nm and 760nm has been commissioned in the summer 2021. This system is installed in the new laser hut (Fig. 2) (right) located in the area formerly used by ATRAP. This new laser system will enable us to excite positronium in Rydberg states via 2 photon resonant processes and to photoionize positronium with principal quantum number  $n=2$ . The spectral bandwidth and duration of the laser pulses are designed to cover a larger fraction of the positronium emitted by implantation of positrons in nanochannel targets. The transfer line guiding the light from the laser hut to the experimental area (Fig. 2) (left) has been commissioned at the end of 2021 and the system is ready for use.

## **Modifications to the control system electronics and software**

To address the challenges posed both by the month-long, round-the-clock parallel running of all experiments with ELENA and by the broad range of physics topics that we intend to cover in the coming years, a complete redesign of both the control system and the underlying electronics was required, which also addresses the issue of long-term maintainability by replacing decade-old custom built electronics by standardized modern commercial systems. Given its central role, the architectural upgrade of the AEGIS experiment control system focused first on the trap control system.

### *Modifications to the control system electronics*

The electronics of the new AEGIS trap control system are based on the Sinara family of hardware [4], while the software running on it is based on the ARTIQ (Advanced Real-Time Infrastructure for Quantum physics) infrastructure [5]. The ARTIQ / Sinara system features a versatile portfolio of open-source software and hardware developed for quantum information research and widely used in atomic physics experiments.

At the core of the ARTIQ ecosystem, the Sinara hardware provides compact, reproducible, modular, and versatile electronics able to steer intricate, time-critical experimental setups. In addition to being optimized for the small amount of space available at the experimental areas of the AD, the use of the standardized Sinara hardware also keeps the control system maintainable in the long term, instead of relying upon homemade, unique solutions for our very specific purposes. The electronics use the DRTIO (Distributed Real Time Input/Output) system for time and data transfer, allowing for stable, high-speed Gbps communication between the devices.

The main ARTIQ control carrier, called Kasli, comprises an Artix-7 FPGA and can control up to twelve extension modules. Kasli itself can be used as a stand-alone core device as well as a repeater or satellite of the DRTIO communication, capable of passing both a connected external clock and the control communication between carriers, thus facilitating straightforward adaptations and extensions of the experiment. Thanks to this flexible adaptability and the modular nature of the Sinara hardware, the control system is rendered future-proof. For the trap control system of the AEGIS experiment, Kasli is combined with digital I/O units and fast DAC modules, called Fastino, from the Sinara repertoire as well as custom-designed 1 MHz high-voltage amplifiers. The high-speed I/O units combine 16 MCX connectors, individually configurable in batches of four, on a single thin module, rendering the provision and reception of trigger signals to and from the entire experimental setup advantageously compact as well as fast. Each Fastino offers the possibility of a 3 Mbits/s digital-to-analog conversion with a 16-bit resolution for 32 channels simultaneously, providing output voltages in the range of  $\pm 10$  V.

The high-voltage amplifier units, which have been specifically designed for the needs of the AEGIS experiment, are each capable of 20-fold amplifying the output voltages of eight of the

respective Fastino channels to up to  $\pm 200$  V. Each amplifier output possesses an individual opto-isolator to prevent a propagation of the noise from the amplifiers to the load connected.

The hardware of the AEGIS trap control system consists of three 50 x 20 x 35 cm electronics crates ( Fig 8), all of which contain at least one of each of the three main Sinara component modules mentioned above and four high-voltage amplifier units. The entire control system setup has been assembled, commissioned as part of the existing electronics, and fundamentally tested in the course of 2021.

The high-voltage output channels of two of the crates (one acting as DRTIO repeater, the other as satellite) are needed to synchronously set the potentials on the electrodes of the 5 T trap region of the experiment, used for antiproton capture and electron cooling, while the third crate provides the control of the 1 T antihydrogen production trap electrodes. In order to enable a sensitive manipulation of the trapped plasmas, the right timing is critical. A reaction to external digital triggers, for example from ELENA, on the order of microseconds, as well as control of the potentials with a nanosecond synchronicity of all involved electrodes, is necessary, which is ensured by the fast signal transfer inside the ARTIQ system.

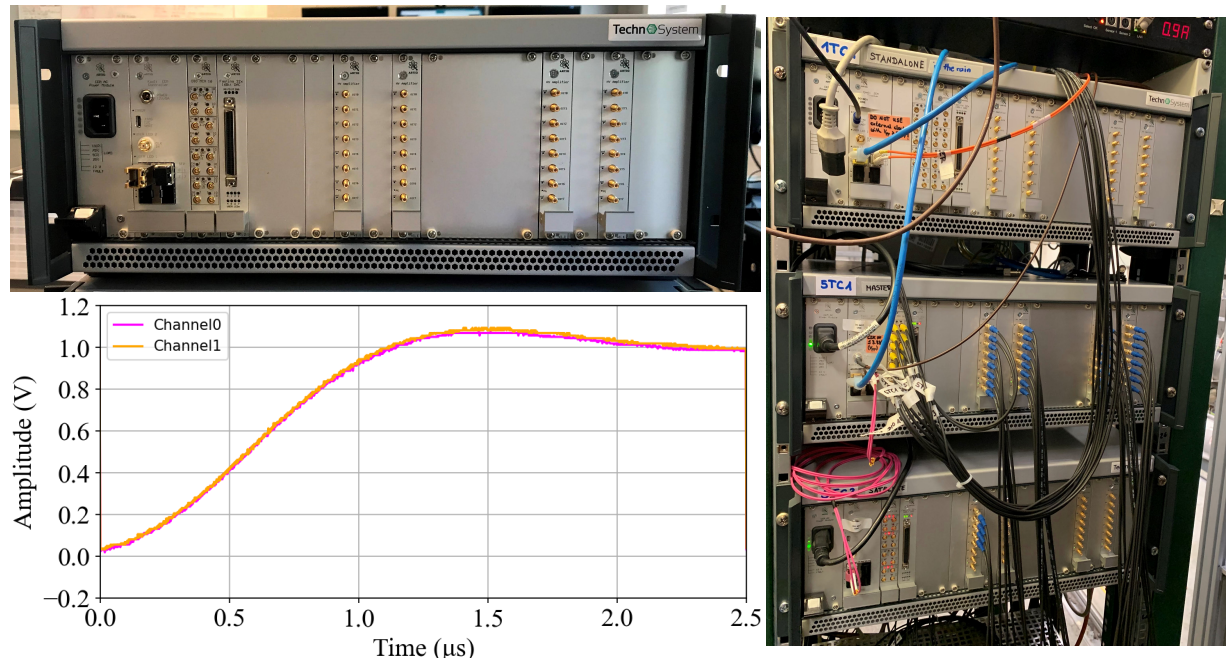


**Figure 8.** Left top: One of three fully equipped AEGIS Sinara crates, including (from left to right) power module, Kasli carrier, digital I/O units, Fastino DAC, and high-voltage amplifiers. Right: All three Sinara crates installed in the main AEGIS electronics rack. Left bottom: Nanosecond synchronicity of two Fastino channel signals programmed to 1 V output.<sup>2</sup>

During the AD/ELENA antiproton beam time in 2021, the fast digital I/O units have been demonstrated to reliably acquire and process the incoming trigger signals, essentially enabling the steering of our trap potentials with the required timing and thus the successful capture of antiprotons. Furthermore, the trap control electronics have also been successfully tested as part of the AEGIS positron system, providing triggers for both the positron preparation sequence and

<sup>2</sup> Nanosecond synchronicity can also be observed when programming the maximum Fastino voltage ( $\pm 10$  V), but 1 V is chosen here for discernibility.

the two lasers used for Positronium excitation (and giving us the opportunity to synchronize the two lasers despite their difference in frequencies).

Figure 8 shows example output signals of Fastino when giving an external trigger to the digital I/O unit and subsequently setting a voltage on two of the Fastino channels.<sup>3</sup> The system reaction time to triggers is on the microsecond scale, and as can be observed, it is clearly possible for the system to provide and to control all output channel voltages with nanosecond synchronicity, satisfying the timing requirements of the AEGIS experiment.

In the course of dedicated tests of the high-voltage amplifiers, it has been confirmed that they deliver the expected 20-fold amplification of the provided voltages within the required time; however, oscillations in the output signal have been observed and the design is being fine-tuned to eliminate these.

Communication with the electronics is facilitated via Kasli's high-speed Gigabit Ethernet port. The commands themselves are formulated in a Python-based, high-level programming language, allowing the semi-experienced programmer to apply the set of straightforward commands without a long familiarization phase and making the run scripts clear and short. This has proved to be extremely useful when having to quickly adapt routines during the beam time.

To further simplify and standardize the procedure for creating the run scripts, we have developed an experiment parent class, called *\_AegisExpOfficial*, from which all routines inherit. This main class contains both the code to initialize and configure the hardware and a library of functions to be used to interact with the hardware and trigger signals, which can then simply be called from the different experiment scripts.

The Sinara hardware is also a central component in the new AEGIS LabVIEW control system software, which connects all integral parts of the experiment. Another Python library, called *TCP\_library* (see the next section), has been created to organize the interfacing with the LabVIEW infrastructure. The LabVIEW system itself has also been established in 2021 and was constitutively tested in-depth during the antiproton run.

### *Modifications to the control system software*

As of 2020, the AEGIS experiment software infrastructure consisted of various independent subsystems (e.g. antiproton trap, positron apparatus, laser systems, detectors) managed by a set of computers running several independently-developed control programs, orchestrated by a self-built common control system to perform coordinated experiments. This approach allowed several development works in the early phases of AEGIS to be conducted simultaneously, ultimately allowing the first demonstration of pulsed antihydrogen production, at the price of a significant amount of expert labor to operate the whole system, and with the necessity of constant monitoring of the individual control programs during the data-taking shifts. With the introduction of ELENA, working conditions have changed significantly, with the beam being delivered 24/7, to all the experiments in the AD simultaneously. If the computers managing the various parts of AEGIS would require constant human monitoring as during the 8 hours shifts of the AD, the toll in terms of workload would triple, leading to the necessity to renounce to part of the beam time given the unavailability of extra workforce.

Therefore, a different paradigm was introduced: a new common control system framework that, at the same time, unifies all the individual control programs in a unique, coordinated distributed system, and increased its reliability and safety by introducing a distributed watchdog system so that it can be left running unattended for extensive periods of time. Indeed, this new

<sup>3</sup> The same results can be achieved for the entire set of Fastino channels, but these numbers are chosen for visibility.

paradigm is founded upon two main pillars: the “everything is a MicroService<sup>4</sup>” approach; and the message-passing distributed system architecture of the well-known Actor Model [6], a standard approach for distributed systems specifically designed for the implementation of large projects. The first concept relies upon dividing the code into independent and autonomous parts, the  $\mu$ Services, each with a clear scope and task. The  $\mu$ Services are meant to be separate applications running asynchronously side-by-side, interacting among each other via a built-in messaging system. The second concept comprises the idea of having an identical process, or actor, running on every machine, named Guardian, which both monitors the status of the other Guardians present on the network and the  $\mu$ Services running in local mode, all implemented as independent actors. Each Guardian supplies a common infrastructure to share messages and data between various  $\mu$ Services and among different computers. On the one hand, this paradigm provides a way to unify all the computers as a single, distributed, entity, and on the other hand it enhances the stability, the reliability, and the safety of the system by having a distributed watchdog system, so that no single component becoming unresponsive can pass unnoticed. The unification of all separate subsystems into a single entity is the key feature to enable the full automatization of the experimental procedures, as high level decision often depend on parameters generated by multiple computers.

This new software framework was realized with LabVIEW<sup>TM</sup> (by NI), a choice motivated by several factors. Most of the pre-existing code of AEgIS was already written in this language and its re-adoption maximized code recycling and minimized the learning curve of the experts. Also, some key hardware components of our experiment are natively interfaced in LabVIEW. Finally, it offers a native implementation of the Actor Model within the so-called NI Actor Framework. During the data taking of the 2021 antiproton beam time, a network consisting of 3 computers running in total 17  $\mu$ Services within the new control framework was brought together and operated continuously throughout the whole beam time period. The framework, albeit still in beta, exhibited a very good stability, with close to 100 % up-time; most importantly, it showed that it is possible to run the experiment in a completely unsupervised manner for all the nights of the data taking, automatically pausing and resuming measurements when detecting handleable exceptions e.g., when there was no beam from ELENA. Resources consumption was low (1 Guardian plus 10  $\mu$ Services took less than 500 MB of RAM), and virtually no overhead from the watchdog system was observed.

Having successfully validated the methodology during the 2021 antiproton run, this control system framework will be further extended in order to autonomously execute the more complex activities foreseen for the 2022 beam time. Several other subsystems will be incorporated into the new framework (the first one, control of the laser system for Ps excitation and manipulation, has already been successfully incorporated after the end of the antiproton run); the interface with the ARTIQ/Sinara ecosystem will be improved with a better error handling; a higher level of integration with the online data analysis will be evaluated. Together with the deployment of the full Sinara hardware setup, this new control system will enable us to optimize the uptime and quality of data taken during the beam time of the 2022 run without overloading the operations’ team, who will in turn use the man-hours to refine the experiment and analyze the data.

## Status of the positron beam line

The occasion of the required removal and re-installation of the entire positron apparatus and the positronium test setup (so that the apparatus could be disconnected from the AD beam line, and reconnected to the ELENA beam line, both running under the positron apparatus) was used in order to perform substantial improvements. These comprised a thorough alignment

<sup>4</sup>  $\mu$ Service in the following

of the beam axis from the positron source to the test chamber with respect to the geometrical center of the radially confining solenoid magnets; an overhaul of the entire vacuum and cryogenic equipment; and re-organization of racks, of the supply of electricity and of the cabling in order to define a sustainable experimental environment. This work was completed in July 2021 and from September onward, the positron system has returned to full operation. The executed optimization work had a very positive effect on the overall performance of the positron system as can be seen in Fig. 9. The intensity of a pulse of positrons upon ejection from the accumulator at 100 eV is shown as a function of the accumulation time for two different years of data taking with the same scintillation detector in the same geometry. The signal obtained at the end of 2021 is almost the same as that achieved in 2017, even though the activity of the radioactive positron source ( $^{22}\text{Na}$ , half-life of 2.6 years) is now three times lower.

As a final step, tests of positronium formation were performed in the dedicated test setup. To prepare for future developments, as several planned experiments with positronium require a field-free region, the main efforts focused on the removal of any magnetic and electric field in the positron/positronium converter region. Positron pulses from the positron system are guided in the direction of the positron/positronium converter by using a magnetic-electrostatic guiding system [7]. In the converter region, two coils have been used in past experiments that generate a magnetic field up to 300 Gauss [8, 9, 10, 11], in combination with a focalization electrostatic lens, in order to optimize the efficiency of the beam transport and to spatially compress the positron cloud on its way towards the target. In the present tests, the two coils were kept off while a fast switcher was used to switch off the focalization electrostatic lens immediately after the positron implantation in the converter occurred. The removal of the magnetic field resulted in a decrease of the transport efficiency of about 15 %, which is acceptable for the planned research.

In Fig. 9 (right, upper panel), the time distribution of gamma rays generated by positrons and positronium annihilations as measured by a  $\text{PbWO}_4$  scintillator in the described transport configuration is shown. The prompt peak in the spectrum is generated by positron annihilations while the long tail to its right comes from the annihilation of the long-lived (142 ns) ortho-positronium atoms emitted into the vacuum. The lower panel shows the potential on the so-called focus lens. The time required by the potential of this lens to go from -3000 V to 0 V is shorter than 30 ns. After this time, the formed positronium expands in a completely field-free environment.

## The 2021 antiproton beam time

The antiproton beam time of 2021 was mainly devoted to re-establishing antiproton detection and catching conditions in the AEGIS apparatus after the many changes introduced with the advent of ELENA, study the effectiveness of the Parylene N degraders and investigate the effectiveness of the new control system software and hardware in handling 24/7 operation of the experiment.

The main tool used to perform most of the 2021 beam time studies was the micro-channel plate (MCP) detector at the end of the apparatus, now doubled in radius with respect to 2018 and featuring a dual imaging and timing readout by means of a CMOS camera imaging the phosphor screen of the MCP and a fast oscilloscope recording its (AC) waveform in time (see Fig. 10 for a visual reference). These were enabled by the deployment, in 2021, of extra configurable triggers from ELENA, which provide accurate triggers well in advance with respect to the bunch arrival, and thanks to the high degree of timing control offered by the Sinara-based trap electronics.

Accurate steering of the ELENA beam was performed by means of the non-destructive SEM grids from the ELENA beam line combined with MCP destructive imaging. The beam could

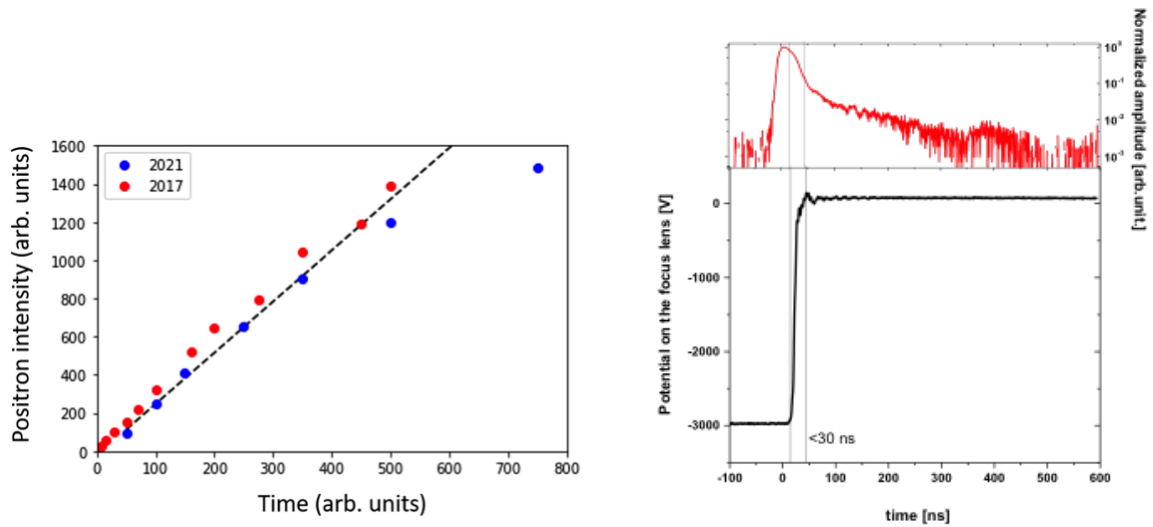


**Figure 9.** Left: Comparison of the positron intensity as a function of the accumulation time for the year 2017 (red) and 2021 (blue). The optimization of the system as detailed in the text led to a similar performance now as was last achieved in 2017, despite a reduction of the source activity of a factor of three. Right: (upper panel) time distribution of gamma rays generated by positron annihilations (prompt peak) and positronium annihilations (tail at the right of the prompt) after positron implantation in the positron/positronium converter; (lower panel) potential on the focus lens.

indeed be imaged as a whole by the enlarged MCP, and steering with both MCP and SEM grids was possible thanks to the small ( $\sim 10\%$ ) losses of SEM detectors. The combination of the two detectors proved to be a fast, accurate and reliable diagnostic of the ELENA beam conditions, and optimal steering conditions from ELENA were found in just a few hours of beam time.

Antiproton degrader studies were performed by inserting the different Parylene N foils at our disposal and measuring the time distribution of antiproton impacts on the MCP by its digitised phosphor electrical signal (Fig. 10, right). The so-obtained time-of-flight distribution of degraded antiprotons  $f(t)dt$  allowed the energy distribution after degrading  $f(E)dE$  to be directly worked out, as shown in Fig. 11. The annihilation signal of antiprotons on the same fast scintillation detector at the beginning and at the end of the apparatus was used to calibrate the method. An example of such energy distributions, obtained with the main  $1.6\ \mu\text{m}$  Parylene N foil degrader, is shown in Fig. 11 (fine-tuning of the antiproton range curve is carried out by variable thickness degrader foils placed outside of the 5 T magnet, see below). Here, the effect of energy degradation from the Parylene N foil is evident as most of the detected antiprotons have an axial kinetic energy of  $30\ \text{keV}$  or lower, with only a small fraction at higher energies and most of the particles in the  $10 - 30\ \text{keV}$  range. These results are in line with the Geant4 simulation predictions discussed above. A long tail at lower energies was also observed, in the trappable range of the high voltage electrodes. Indeed, the higher electrodes allowed to alter the time-of-flight distribution of antiproton preventing the annihilation on the MCP of the slowest fraction (Fig. 11, right).

Antiprotons from this slow tail could indeed be trapped, similarly to what was routinely done with the degraded AD beam, between our HV1 and HV3 electrodes in the 5T region of our experiment (for a total trapping length of about 80 cm), operated at its nominal 5T field in place of the 4.46T used in the past. The high voltage system allowed potentials of up to 10 kV to be set on the electrodes, trapping close to 100 % of antiprotons emerging from the degraders in the

0 – 10 keV energy range. Antiproton catching was quickly established and detected on external counting scintillators, mainly thanks to the versatility of the new control system deployed in 2021. Fig. 12 thus shows the antiproton annihilation rate as a function of time for such a trapping and controlled annihilation sequence: the pulse at 9s corresponds to the annihilation of incoming antiprotons; the broad peak starting at 13s comes from a controlled ramp-down of the trapping voltage over around 10 seconds, on which a pion burst at 17s is superimposed. Trapping experiments were routinely performed at different electrode closing times and voltages to find the optimal catching conditions.

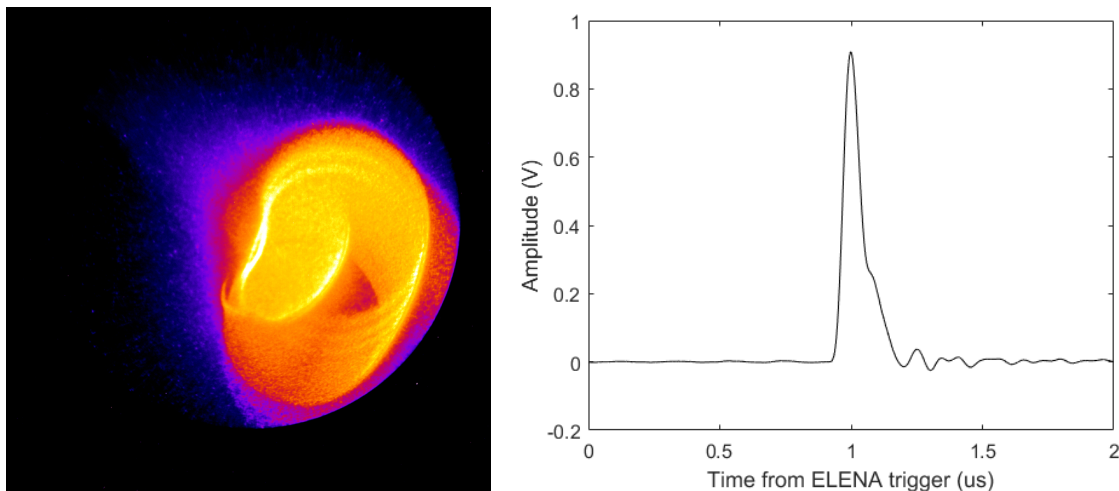


**Figure 10.** Left: the ELENA antiproton beam as detected by the MCP+phosphor+CMOS detector at the end of AEgIS. Right: raw waveform of the antiproton beam annihilations on the MCP surface, obtained by recording the decoupled AC signal of the MCP phosphor screen.

Studies with the variable thickness thin degrader foils (consisting of multiples of 100 nm Parylene N foils) were conducted to measure the frictional cooling and energy loss in these thin Parylene N foils, to probe the accuracy of Monte Carlo numerical estimates and to determine the optimal degrading thickness for 2022 and after. These studies showed that a roughly 20 % reduction of the beam energy for every 100 nm of added Parylene N foil can be obtained, at the price of a modest beam intensity reduction.

Finally, experiments with negative hydrogen ion bunches from ELENA were conducted to assess the feasibility of conducting further studies with protonic systems and anions inside AEgIS. Negative hydrogen ion bunches entered the 5T and 1T apparatuses similarly to antiprotons and were successfully imaged and steered with the MCP detector sited inside the 1T magnet at the end of the internal electrodes in the absence of any intermediate degrader foils. Inserting these allowed a study of electron stripping by impacting the ions on the thin Parylene N foils, showing that this method is able to provide a 100 ns-long pulsed source of protons in the 1 – 10 keV range suitable, for instance, for the first protonium formation experiments inside AEgIS.

The whole data taking campaign was a success from the point of view of field-testing the new control system, both from the hardware and software points of view. The system allowed a 100% up-time both during the day (supervised work) and during the night (unsupervised work). The ARTIQ/Python software interface met our expectations in terms of fast development of experimental procedures, allowing flexibility, fast debugging and effectively dealing with the complexity of the experimental procedures, while the LabVIEW control system provided a

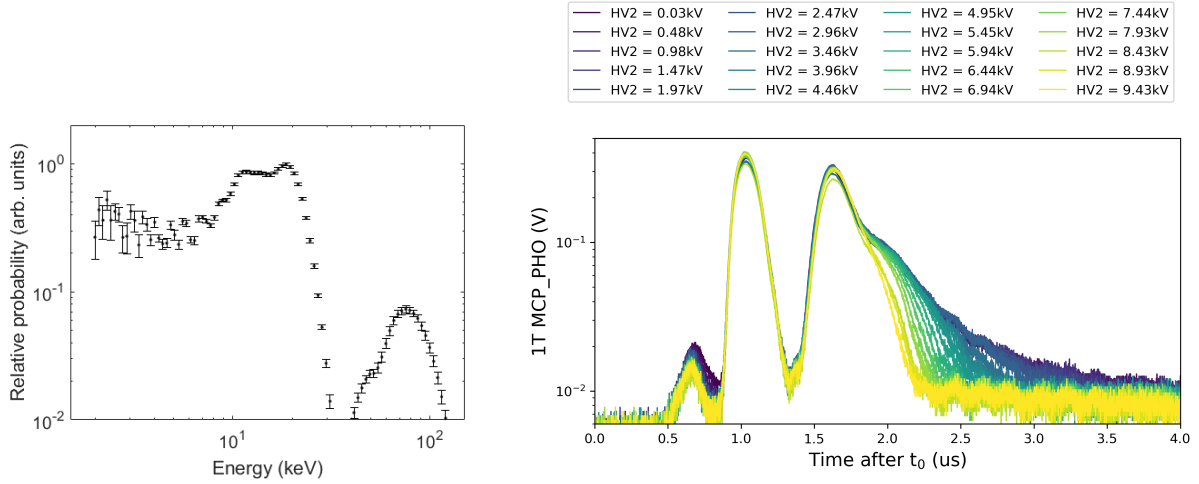


**Figure 11.** Left: Energy distribution of antiprotons after degrading in a  $1.6 \mu\text{m}$  Parylene N foil degrader and obtained from their time-of-flight detected by the MCP detector (details in the text). Right: stopping of the slowest antiproton tail by the high-voltage electrodes used for catching for different values of the trapping voltage.

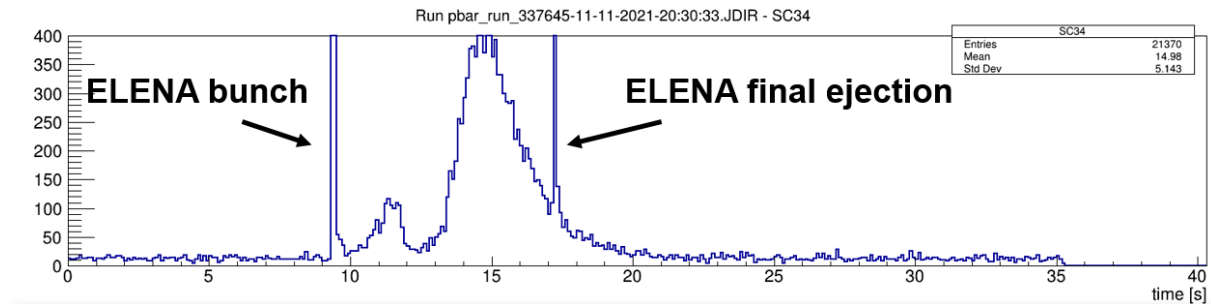


**Figure 12.** Antiproton trapping, immediate release and detection on external scintillation detectors during the 2021 antiproton run. The catching traps in the 5T region were routinely operated at 10 kV trapping voltage.

solid and reliable basement for interfacing to the whole experiment distributed system. Good scalability and performance is also to be reported. In conclusion, it proved to be a major improvement with respect to the former approach, leading to stable around the clock operation with a reduced operations team and much faster development iterations.

### Auxiliary developments

Efficient beam formation and gravity measurements through the envisioned AEGIS techniques both require the capability to rapidly deexcite the initially formed Rydberg antihydrogen atoms. Theoretical studies have identified light-induced Rydberg state mixing and laser deexcitation techniques to be efficient for this purpose [12]. They allow to decrease the effective lifetime of the initially formed states toward the ground state by several orders of magnitude to some tens of microseconds, bringing a substantial amount of the initially formed Rydberg atoms into the ground state right in the formation region. After initial tests on a beam

of excited cesium atoms, THz light sources were identified to be appropriate for state mixing [13]. The experimental demonstration of fast stimulated deexcitation in a beam of hydrogen atoms was initiated at CERN in 2021. The hydrogen beamline consists of a source of mainly ground-state hydrogen atoms, obtained from the dissociation of molecular gas in a microwave discharge plasma, and a set of vacuum chambers, see Fig. 13. The first chamber is coupled to a pulsed Ti:Sa laser for excitation to Rydberg states. The second chamber hosts the detection apparatus namely an electric field ionizer and a pair of Chevron stack microchannel plates. A two-stage thermal shield cooled by a cryocooler allows to prevent blackbody radiation from acting upon the hydrogen quantum states under investigation. A new laser laboratory was built in building 275 to host the beamline. Substantial delays were introduced by constraints due to the pandemic. Despite these drawbacks, the beamline has been successfully set up and the laser could be commissioned in fall 2021 now generating average pulse energies of 10 mJ at the required 364 nm ( $n=2 \rightarrow n=30$ ) wavelength. A second possibility to obtain Rydberg states for deexcitation studies is to rely on collisional and recombination processes inside the discharge plasma. The presence of Rydberg states with principal quantum numbers of interest was readily evidenced. The signal will allow for first trials of deexcitation in early 2022. We plan to proceed with both avenues outlined above toward hydrogen Rydberg state production. Laser excitation is more favorable for the commissioning of deexcitation techniques since it allows to generate specific quantum states. In contrast, the distribution of Rydberg states emitted from the discharge better reproduces the conditions faced in an antimatter experiment. Developments of both photomixing technology that is customized to the antihydrogen state-mixing requirements identified theoretically and a deexcitation laser have been initiated and will be carried on in 2022. We plan on a mixing/deexcitation hydrogen proof-of-principle result throughout 2022 which would then allow for a relatively swift installation of the equipment at the AD.

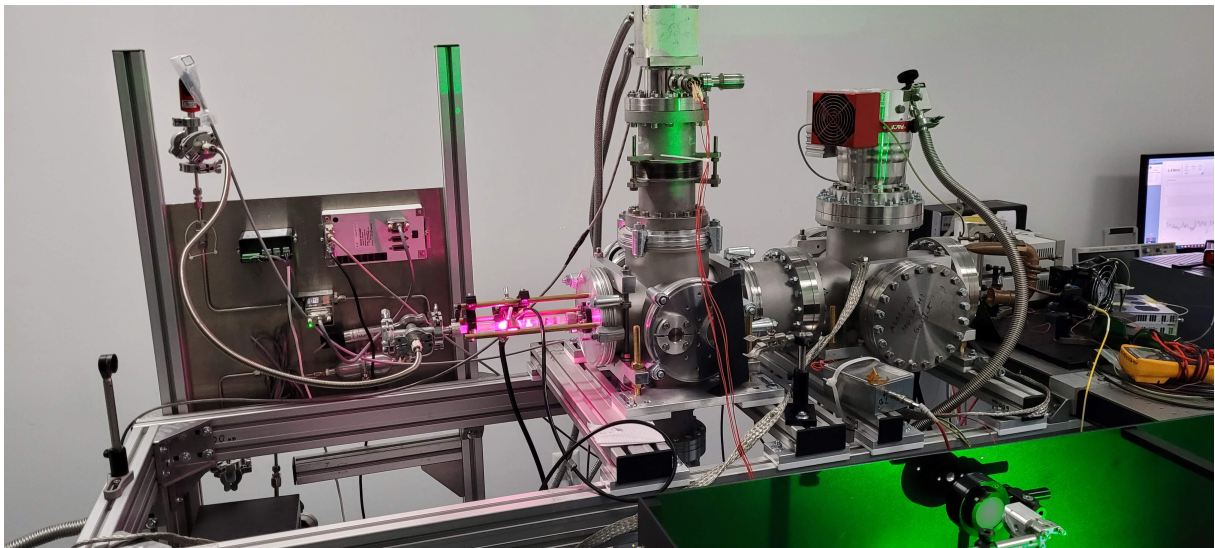


**Figure 13.** Photo of the hydrogen deexcitation setup:  $H_2$  is dissociated (pink glow) within a microwave discharge plasma. Thermal atomic hydrogen emerges from the plasma region and is emitted into the downstream vacuum region via an aperture. The first chamber has laser access for Rydberg excitation (green light shown in the picture originates from the pump laser beam at 532 nm). The second chamber hosts the detection apparatus for measuring the quantum state distribution and a window for coupling the beam to the deexcitation light.

## Summary and beam request

In spite of the continued challenges posed by the Covid-19 situation, we have made and tested a number of major changes to the apparatus in 2021. These activities have prepared the physics program of 2022 and the subsequent years, not least in the manner of working that will be affected by the availability of antiprotons around the clock, and which requires a major step forward in automation and remote operability of the experiment. This was successfully implemented in the full experiment and successfully tested in the antiproton measurement campaign that was run by a very small team in November of 2021.

While some delays have thus accrued, thanks to rescheduling and re-prioritization where necessary, we successfully tested in the 2021 antiproton run most of the modifications that will be required for the physics runs of 2022 and subsequent years and are on track for the final modifications of the apparatus being ready for the 2022 run. For 2022, we thus request a pro-rata access to antiprotons from ELENA for the foreseen duration of the 2022 antiproton beam time.

## References

- [1] CERN-SPSC-2007-017 ; SPSC-P-334 (<http://cds.cern.ch/record/1037532>)
- [2] S. Aghion et al. (AEgIS Collaboration), "Pulsed production of antihydrogen", *Nature Comms. Phys.*, 4:19 (2021)
- [3] CERN-SPSC-2019-043; SPSC-P-334-ADD-1 (<http://cds.cern.ch/record/2692828>)
- [4] G. Kasprowicz *et al.*, "ARTIQ and Sinara: Open Software and Hardware Stacks for Quantum Physics", 2020, publ. Optical Society of America, OSA Quantum 2.0 Conference, 2020, pg. QTu8B.14 (<http://www.osapublishing.org/abstract.cfm?URI=QUANTUM-2020-QTu8B.14>)
- [5] S. Bourdeauducq *et al.*, "ARTIQ 1.0", 2016, publ. Zenodo, (<https://doi.org/10.5281/zenodo.51303>)
- [6] C. Hewitt, P. Bishop and R. Steiger, "A universal modular ACTOR formalism for artificial intelligence", *Proc. Int. Joint Conf. on Artificial Intelligence*, 1973, 235-245.
- [7] S. Aghion et al., (AEgIS collaboration), "Positron bunching and electrostatic transport system for the production and emission of dense positronium clouds into vacuum", *NIMB* 362, 86 (2015)
- [8] S. Aghion et al., (AEgIS collaboration), "Laser excitation of the n=3 level of positronium for antihydrogen production" *Phys. Rev. A* 94, 012507 (2016)
- [9] S. Aghion et al. (AEgIS Collaboration), "Producing long-lived  $2^3S$  positronium via  $3^3P$  laser excitation in magnetic and electric fields", *Phys. Rev. A* 98, 013402 (2018)
- [10] C. Amsler et al., (AEgIS collaboration), "Velocity-selected production of  $2^3S$  metastable positronium", *Phys. Rev. A* 99, 033405 (2019)
- [11] M. Antonello et al., (AEgIS collaboration), "Efficient  $2^3S$  positronium production by stimulated decay from the  $3^3P$  level", *Phys. Rev. A* 100, 063414 (2019)
- [12] T. Wolz, C. Malbrunot, M. Vieille-Grosjean, and D. Comparat, *Phys. Rev. A* 101, 043412 (2020)
- [13] M. Vieille-Grosjean, E. Dimova, Z. Mazzotta, D. Comparat, T. Wolz and C. Malbrunot, *The European Physical Journal D*, 75, 27 (2021)